CHAPTER 6

PETROLOGY OF MAFIC GRANULITE

Representative samples of mafic granulite were studied and described in this chapter. Based on the mineralogy mentioned below, the mafic granulite is separated into two different categories viz. two pyroxene granulite and garnet-pyroxene granulite. Both these variety are common in EGP and their occurrences are discussed in chapter 3 and their locations are given in Table 6.1. Importantly, beyond variations in silicate phases, these varieties also demonstrate disparities in oxide, sulphide, and sulphate phases. The presence of oxides and sulphides is documented across different modes in both types. To provide an intricate portrayal of their detailed petrography, the textural observation is subdivided into three sections delineating the assemblages as silicate-oxide, oxide-sulphide, and sulphide-sulphate.

6.1 Silicate-oxide phases

6.1.1 Two pyroxene granulite

This particular type of mafic granulite samples was collected from Anantagiri (17EG14), Muliyaguda (17EG16), Loteru (9C), and Duruva (17EG22) regions of central EGP and from Dimrijholi (PLB71A), Charichhak (PLB89B) region of northern part of EGP. The rock is composed of orthopyroxene (Opx) + clinopyroxene (Cpx) + plagioclase (Pl) + K-feldspar (Kfs) + hornblende (Hbl) + biotite (Bt) + ilmenite (Ilm) + apatite (Ap) ± magnetite (Mag) ± sulphides ± quartz (Qtz) is found in equal abundances. These minerals show granoblastic texture throughout. The rock has been described based on the textures involving silicate-oxide-sulphide-sulphate phases.

The modes of occurrence of oxide minerals represented by ilmenite (Ilm) and magnetite (Mag) are variable, and are described under the following four categories:

1) Oxide phases that occur as inclusions inside porphyroblasts, designated Ilm_1 and Mag_1,

2) Oxide phases that are next to porphyroblastic phases and exist as separate grains, are described as Ilm_2 and Mag_2.

3) Mag_3, term is used to infer magnetite that forms when pyrrhotite is replaced by sulphide phase, like pyrite, and

4) Mag_4, indicate magnetite filling fractures in the form of thin veins with a thickness of 2-6 μm (Fig. 6.1).

In sample 17EG14, exsolved lamellae are present in both orthopyroxene and clinopyroxene, whereas discrete ilmenite (Ilm_2) grains are mostly free from such exsolved structures. Ilm_2, with a size greater than 400 μm along its maximum dimension, is found in close proximity to porphyroblastic orthopyroxene and clinopyroxene (Fig.6.2). Plagioclase grains exhibit a porphyroblastic texture with deformed twin lamellae. At some places, plagioclase grains show evidence of recrystallization, transforming into smaller, strain-free grains along the margins. Micro-veins of K-feldspar are occasionally observed along the grain boundaries of plagioclase. Furthermore, a discontinuous thin film of K-feldspar can be seen along the margin of pyroxene grains (Fig.6.3). Within plagioclase, patches of K-feldspar form antiperthite texture (Fig.6.4). Along the boundary between K-feldspar and plagioclase, myrmekitic intergrowth has formed.

The sample 17EG16 shows a similar assemblage, and the minerals exhibit evidence of recrystallization, which imparts a weak gneissic fabric to the rock. Common features include marginal granulation and stretching occurring along the foliation of the porphyroblastic grains. The smaller feldspar grains exhibit recrystallization, characterized by annealed polygonal grain boundaries. A noteworthy aspect of this assemblage is the presence of exsolved hematite lamellae within the ilmenite (known as hemo-ilmenite: Ilm_2), alongside some discrete lamellae-free Ilm_2 and Mag_2. In certain areas, the lamellae-free Ilm_2 grains partially engulf granular Mag_2 (Fig.6.5). In some instances, fine trellis intergrowth of hematite is observed in Ilm_2, but it does not cover the entire grain where the Ilm_2 grains are in contact with Mag_2 (Fig.6.6). Conversely, when Ilm_2 comes into contact with porphyroblastic pyroxene, it displays the presence of as many as two successive generations of exsolved lamellae (Fig. 6.7). Mag_2, with a thickness ranging from 3 to 10 μm, often occurs as tripartite grains alongside hemo-ilmenite and pyrite within the feldspathic matrix (Fig.6.8). Local occurrences of both Mag_1 and Ilm_1 (without lamellae) inclusions are found within porphyroblastic clinopyroxene, separated from the host by a quartz rim (Fig.6.9). Sample 9C includes hornblende in its mineral assemblage. Additionally, hornblende is observed as patches on the porphyroblastic orthopyroxene. Along the grain boundaries of biotite and porphyroblastic hornblende, tiny recrystallized orthopyroxene grains are present (Fig.6.10). Ilm_1 grains are present as inclusions within the porphyroblastic phases and exhibit hematite exsolution lamellae. Bipartite grains of Mag_2 with Ilm_2 (containing exsolved hematite) are found along the margin of porphyroblastic orthopyroxene grains. The occurrences of Mag_2 close to patchy hornblende and retrograde biotite are a notable feature (Fig.6.11). Sample 17EG22 exhibits a gneissic fabric, with orthopyroxene and clinopyroxene grains containing exsolved lamellae of each other. Marginal granulation of the porphyroblastic phases is commonly observed. The perthitic feldspar displays a myrmekitic texture (Fig.6.12). In the leucosome layer, cuspate grains of quartz and feldspar are present (Fig.6.13). Ilm_2 grains in this sample do not contain exsolved hematite. Although no discrete Mag_2 is found in this sample, Mag_3 grains are locally observed in contact with pyrite.

On the contrary Sample PLB71A contain deformed feldspar and pyroxenes. Both Cpx and Opx are deformed and stretched locally. A few feldspar grains show primary twinning but the fine-grained feldspathic matrix show recrystallization. Ilm_2 grains are free of hematite lamellae. However, discrete Mag_2 grains are found in contact with porphyroblstic Opx grains. Sample PLB89B also contain hornblende that occur as patch within porphroblastic pyroxene grains. A few orthopyroxene grains contain biotite inclusion. Locally Opx and Hbl contain fine to thick corona of Ilm_2.

6.1.2 Garnet-pyroxene granulite

The three mafic granulite samples from Arlaput (17EG23), Baldah (17EG24) and Chhatrang (PLB93A) belong to this category. Here, garnet is present alongside orthopyroxene, clinopyroxene, plagioclase, and ilmenite, forming porphyroblastic phases. Additionally, these samples contain quartz, biotite, hornblende, K-feldspar, apatite, sulphide, sulphate phases, and a trace amount of calcite. The leucocratic layer is primarily made up of quartz, K-feldspar, and plagioclase, while the melanocratic layer comprises garnet, orthopyroxene, and clinopyroxene. Garnet appears in two different textural modes in these samples: (i) as a porphyroblast in sample 17EG23 and (ii) as a reaction corona, either with or without intergrown quartz, separating porphyroblastic orthopyroxene and clinopyroxene from plagioclase in sample 17EG24 (Fig.6.14). The rocks show clear evidence of grain-scale deformation, characterized by recrystallization and the formation of quartz ribbons, deformed feldspar grains, and a relatively stretched nature of the porphyroblastic phases. Clinopyroxene grains display exsolved lamellae of orthopyroxene (Fig.6.15). Ilm_2 grains, in their discrete form, are free of exsolved hematite. However, discrete Mag_2 grains are absent, while Mag_4 occurs along fractures. On the other hand, Sample PLB 93A is not migmatitic in appearance but it is highly recrystallized and giving a fine appearance. The porphyroblastic garnet (50-80 µm in length) and Cpx grains (100-150 µm in length) along with Ilm_2 are stretched along the foliation (Fig. 6.16). Often quartz and feldspar grains locally form ribbon like structure. The occurrence of sulphide grains is relatively rare in these samples.

6.2 Oxide-sulphide phases

Three distinct types of sulphide phases are found in the samples: pyrrhotite (Po), pyrite (Py), and chalcopyrite (Cp). Both pyrite (Py) and chalcopyrite (Cp) grains are associated with pyrrhotite (Po) grains. Texturally, there are two different types of pyrite present in the assemblages. The first type, larger pyrite grains (Py_1), are in equilibrium contact with Ilm_2 and Mag_2, forming the peak metamorphic assemblage (Fig.6.17). The second type of pyrite (Py_2) occurs as a replacement along the margin of pyrrhotite (Po), either with or without Mag_3. In sample 17EG14, pyrrhotite (Po) is the dominant sulphide phase. In certain places, Py_1 is present as a remnant within the Po grains, and noteworthy exsolved blebs of Cp are observed (Fig.6.18). All these sulphide phases are found in association with exsolution-free Ilm_2. In sample 17EG14, there is no occurrence of magnetite grain (in any form) associated with the sulphide phases. Conversely, in sample 17EG16, Py dominates over Po, while Cp is the other sulphide phase. Po is occasionally seen as a relict within the Py_2 grains or is replaced by both Py_2 and Mag_3 (Fig.6.19). In this case, both Py_2 and Cp are associated with the hemo-ilmenite (Ilm_2) and magnetite (Mag_2) grains within the silicates (Fig.6.8). Mag_4 occurs as intergranular fracture filling veins with a thickness of 2–4 μm and is frequently seen partially engulfing Po grains. In sample 17EG22, the sulphide phases, primarily dominated by Po, are found in close association with Ilm_2. In certain areas, Py_2 and Mag_3 are observed replacing Po (Fig.6.20). Additionally, there are local occurrences where Cp and Po display a convolute mutual boundary (Fig.6.21). In sample 9C, pyrite (Py) and chalcopyrite (Cp) grains are present, with rare occurrence of pyrrhotite (Po). A noteworthy aspect is the patchy alteration of Py to a mixture of K, Fe, Si, Al, and S, which has been confirmed by SEM-EDS analysis. Within this alteration, tiny grains of Py and Cp are observed as relics, while Py_1 is accompanied by a mantle of Mag_3 (Fig.6.22). In samples 17EG23 and 17EG24, sulphide phases are less prominent. Locally, Py_2 grains are found along with Mag_3 in a quartzofeldspathic matrix containing relics of both Cp and Po. It is common to find fracture filling veins of Mag_4 and Mag_3 rims over Py_2. Additionally, in certain areas, patchy veins of Py_2 occur along intragranular fractures of plagioclase. The sample PLB71A contain only chalcopyrite as sulphide phase beside oxides. On the contrary, PLB89B and PLB93A are devoid of sulphide phases.

Based on their textural features, two distinct sulphide-oxide associations have been categorized.

1. The Py-dominated association, where pyrrhotite (Po) appears as remnants within pyrite (Py); magnetite vein (Mag_4) is replaced by pyrite; Py_2 forms rims over Po; and hemo-ilmenite (Ilm_2) occurs as separate grains.
2. The Po-dominated association, where discrete pyrrhotite (Po) grains are found in association with plagioclase and hemo-ilmenite (Ilm_2); pyrite (Py_1) is observed as relics within Po, and there are no discrete grains of magnetite (Mag_2) or lamellae of hematite within Ilm_2. Chalcopyrite is commonly present in both associations.

6.3 Sulphide-sulphate phases

In sample 17EG24, pyrite (Py_1, Py_2) occurs with barite. The latter phase occurs in three different textural modes: (1) barite replacing pyrite grains within plagioclase (Fig.6.23), (2) barite occurring as discrete grains within calcite along the quartz-feldspar grain contacts (Fig.6.24), and (3) barite forming thin veins with a width varying from 2 to 5 µm, occurring within plagioclase and K-feldspar (Fig.6.25). In certain areas, Fe-oxide inclusions have been observed within barite. Moreover, a partial rim of barite surrounding small mixtures of sulphide-sulphate has been found, with their compositions only identified through EDS analysis.

6.4 Mineral Chemistry

6.4.1 Two pyroxene granulite

In sample 17EG14, orthopyroxene exhibits a slightly Mg-rich composition, with an X_{Mg} [(Mg/(Fe^{2+}+Mg)] ranging from 0.53 to 0.55. Alumina content of orthopyroxene varies from 0.98 to 1.21 wt.%, as shown in Table 6.2. Clinopyroxene is magnesian, with $X_{Mg} \sim 0.70$. The alumina content of clinopyroxene decreases from the core (2.28 wt.%) to the rim (1.67 wt.%). Plagioclase ($X_{An} = 0.73$) is calcic. Ilmenite (Ilm_2) grains display low but variable proportions of hematite ($X_{Hem} = 0.05$) and geikielite ($X_{Geik} = 0.03$) components. Additionally, Ilm_2 grains contain Barium (Ba) in the range of 0.87 to 1.12 wt.% BaO. A patch of K-feldspar, containing up to 0.68 wt. % BaO, is observed within plagioclase, and it displays patchy zoning as revealed by X-ray mapping (Fig.6.26a and b). Along the boundary of this patchy K-feldspar, there is evidence of Na-loss, accompanied by a gain of Ca. K-feldspar micro-veins exhibit slightly higher Ba concentration, reaching up to 0.96 wt.% BaO.

In sample 17EG16, orthopyroxene exhibits a slight Al-enrichment, with its alumina content increasing from 1.21 wt.% at the core to 1.41 wt.% at the rim. On the other hand, clinopyroxene (X_{Mg} = 0.75) demonstrates a decrease in Al content, ranging from 3.15 wt.% at the core to 2.74 wt.% at the rim. Plagioclase is rich in calcium, with X_{An} of 0.72. Ilmenite (Ilm_2) comprises a small fraction of hematite (X_{Hem} = 0.3–0.4), which is comparable to the ferrosilite component found in orthopyroxene (X_{Fe} = 0.42). The presence of the geikielite component is minor (X_{Geik} = 0.035−0.046), but ilmenite contains Barium (Ba) in the range of 0.85–0.96 wt.% BaO. Ilm_1 also exhibits a similar composition. Magnetite inclusion (Mag_1) within clinopyroxene and discrete magnetite grains (Mag_2) exhibit a similar chromium content, ranging from 0.37 to 0.36 wt. % Cr_2O_3. In contrast, the magnetite rim (Mag_3) contains a higher chromium content of 0.64 wt. % Cr_2O_3. The magnetite vein (Mag_4) shows a very low chromium content of 0.02 wt. % Cr_2O_3. Magnetite inclusion (Mag_1) within clinopyroxene displays a slightly higher titanium content (Table 6.2) compared to Mag_2 and the magnetite vein (Mag_4).

Orthopyroxene (X_{Mg} = 0.61) and clinopyroxene (X_{Mg} = 0.77–0.81) both exhibit Al-enrichment in sample 9C (1.44–1.51 wt. % Al_2O_3) from core to rim. Plagioclase is calcium-rich, with X_{An} of 0.81. Hornblende (magnesio-hastingsite) shows a slight Mg-enrichment from core to rim, with an X_{Mg} ratio ranging from 0.64 to 0.67. Typically, patchy hornblende tends to be more magnesian. Ilmenite contains a significant amount of hematite (X_{Hem} = 0.11) but has a low geikielite component (X_{Geik} = 0.02). Ilmenite lamellae within hematite also contain Barium (Ba) in the range of 0.84–0.88 wt.% BaO. Late biotite is magnesian, with X_{Mg} of 0.71.

In sample 17EG22, orthopyroxene is less magnesian, with an X_{Mg} of 0.45. Its alumina content shows enrichment from the core to the rim, ranging from 0.9 to 1.3 wt.% Al_2O_3. On the other hand, clinopyroxene (X_{Mg} = 0.64) contains higher alumina content at the core. Plagioclase is rich in anorthite (X_{An} = 0.60). In antiperthite, K-feldspar is Na-poor, but it contains slightly higher Na when it occurs as a host in perthite (X_{Ab} = 0.11). Ilmenite exhibits low hematite (X_{Hem} = 0.03) and geikielite (X_{Geik} = 0.01) contents. Small amount of Ba is present in this mineral, ranging from 0.87 to 0.94 wt.% BaO. Pyrrhotite grains contain no other elements like Zn or Cu, and the X_{FeS} content was calculated to be 0.88.

6.4.2 Garnet-pyroxene granulite

In sample 17EG23, the compositional differences in porphyroblastic garnet are denoted as $Alm_{58–59}$ $Prp_{18–19}$ $Grs_{18–19}$ $Sps_{2–3}$. Compositional difference in plagioclase is observed, with the anorthite component decreasing from a core (X_{An} = 0.42) to rim (X_{An} = 0.39; Table 6.3). Clinopyroxene is magnesian (X_{Mg} = 0.74) with alumina content varying from 1.54 wt.% to 1.73 wt.%. Ilmenite contains Ba (0.94 wt.% BaO) and a minor amount of hematite (X_{Hem} = 0.02), but notably includes a substantial geikielite component (X_{Geik} = 0.24). Biotite (X_{Mg} = 0.7) inclusions within the garnet shows notably high Ti content, reaching up to 5.4 wt.%. Garnet in sample 17EG24 shows a composition of $Alm_{58–60}$ $Prp_{16–19}$ $Grs_{17–19}$ Sps_{2}. Plagioclase composition shows variability, ranging from $Ab_{42–59}$ $An_{39–52}$ $Or_{1–2}$. The core of the plagioclase is calcic (X_{An} = 0.52), while the rim is more albitic (X_{An} = 0.42). Clinopyroxene is magnesian (X_{Mg} = 0.71 to 0.77), and shows decrease in alumina content towards the rim. Ilmenite contains a low but varying amount of hematite (X_{Hem} = 0.03–0.06), and geikielite component (X_{Geik} = 0.04). It also shows a reduction in BaO content from core to rim. Patchy zoning in plagioclase is present at the perthitic feldspar contact which is evident from the Ca and Na mapping (Fig.6.26).

6.5 Mineral reactions

The progression of the two mineral assemblages can be most accurately elucidated by tracing the sequential emergence of silicate, oxide, and sulphide minerals through a series of mineral reactions. A crucial element of this evolution is the introduction of garnet, which exclusively manifests within garnet-pyroxene granulite and holds significant importance as a silicate mineral within this context. The dominant mineral combination in two pyroxene granulite includes orthopyroxene + clinopyroxene + plagioclase + K-feldspar + ilmenite (Ilm_2) ± magnetite (Mag_2), as well as sulphide minerals (Py_1 + Po and ± Cp). Notably, the occurrence of ilmenite in two pyroxene granulite is largely in the form of separate grains (referred to as Ilm_2) and is notably devoid of hematite exsolution when in contact with pyroxene grains. This characteristic is observed in samples 17EG14 and 17EG22. Importantly, both of these samples lack distinct magnetite grains (referred to as Mag_2). Also, the same character is noteworthy for garnet-pyroxene granulite. The ilmenite grains in question possess an insignificant amount of hematite. Within two pyroxene granulite, there are bipartite grains of Ilm_2 (with/without hematite lamellae) – and Mag_2. These occurrences are observable adjacent to orthopyroxene (Fig. 6.5 and 6.6). Mag_2 lacks ilmenite lamellae and exhibits a low Ti content (TiO_2 < 1 wt. %), implying a minimal presence of the ulvöspinel component. In sample 17EG16, Ilm_1 within clinopyroxene is devoid of hematite exsolution, while Ilm_1 within porphyroblastic hornblende in sample 9C does contain hematite lamellae. The chemical data for these phases reveal no significant compositional differences between Ilm_1 and Ilm_2. Hence, it is probable that the ilmenite was inherited from lower-grade assemblages. The presence of Ilm_2 (Hemo-ilmenite) and Mag_2 along the margin of orthopyroxene can be accounted by the subsequent reaction, which almost certainly occurred at the same time:

$6FeSiO_3 + O_2 = 2Fe_3O_4 + 6SiO_2$ …………………………. (6.1).

(in Opx) Mag_2 Qtz

$4FeSiO_3 + O_2 = 2Fe_2O_3 + 4SiO_2$ ………………………….. (6.2)

(in Opx) (in Ilm_2) Qtz

Reactions (6.1) and (6.2) took place within an oxidized environment, as evidenced by the presence of hematite exsolution lamellae ranging from fine to coarse (multiple sets) within the ilmenite crystals.

This particular texture has been documented in various granulite terranes within the region, as outlined in earlier studies (Harlov and Hansen, 2005; Bose et al., 2009). It is likely that the exsolution process occurred at temperatures lower than 700°C within the $FeTiO_3$–Fe_2O_3 phase transition boundary (Lindsley, 1973, 1991; Ghiorso, 1990; Burton, 1991; Haggerty, 1991). The presence of sulphide phases alongside these oxide compositions is of particular interest. In cases where Mag_2 is not present and Ilm_2 has low hematite content (X_{Hem}^{Ilm} = 0.01–0.03), this latter phase is found in conjunction with Fe-rich orthopyroxene (X_{Opx}^{Fe} = 0.45–0.55, Fig.6.28) and pyrrhotite. Pyrrhotite is the predominant sulphide, surpassing pyrite and chalcopyrite in abundance. In contrast, Ilm_2 contains a hematite component (X_{Hem}^{Ilm} = 0.09–0.11) within samples 17EG16 and 9C, where Mag_2 coexists with pyrite and orthopyroxene. In sample 17EG16, pyrrhotite is the predominant sulphide, often accompanied by chalcopyrite. In the case of sample 9C, orthopyroxene demonstrates a higher magnesian composition (X_{Mg}^{Opx}= 0.62–0.64) compared to sample 17EG16 (X_{Mg}^{Opx}= 0.54–0.57). The presence of pyrrhotite and pyrite alongside the rhombohedral oxide phases is contingent upon the prevailing oxidation conditions, as elucidated by Hall (1986) in his diagram (Figure 1). Hall's work demonstrates that pyrite can exist alongside magnetite under relatively higher oxygen fugacity (fO_2), while pyrrhotite coexists with magnetite under conditions of lower fO_2. As indicated by the oxide-sulphide occurrences, pyrite (Py_2) with or without Mag_3 exhibited marginal growth adjacent to pyrrhotite grains, or pyrrhotite was found as remnants within Py_2. This suggests a chronological sequence where pyrite formed later than pyrrhotite. The possible reaction is

$6FeS_{1-x} + (2-x) O_2 + xSO_2 = 3FeS_2 + Fe_3O_4$ …………………. (6.3)

Po $\quad\quad\quad\quad\quad\quad\quad\quad\quad$ Py_2 $\quad$ Mag_3

This reaction took place under elevated fO_2 conditions (accompanied by a slight rise in SO_2 levels) during the regressive phase, as evidenced by the formation of fine Py_2 within coarse Po grains. The significant metamorphic fluids containing sulfur comprise SO_2, H_2S, and COS (Ohmoto and Kerrick 1977; Frost et al. 1988). COS assumes significance as a sulfur-carrying compound within a fluid environment abundant in CO_2 but lacking in H_2O. The absence of CO_2-carrying minerals in the mafic granulites suggests that COS presence is minimal during the retrogressive phase. In this context, the other two species might exert noteworthy influences.

In sample 17EG16, pyrite (Py_2) is closely linked with Mag_2 and hemo-ilmenite (Ilm_2) in tripartite grains, a phenomenon attributable to the subsequent reaction:

$Fe_3O_4 + 6H_2S + O_2 = 3FeS_2 + 6H_2O$ ………………. ….. (6.4)

Mag_2 $\quad\quad\quad\quad\quad\quad$ Py_2

Conversely, Py_1 is found within Mag_3 in sample 9C (Fig. 6.22), which points to a late-stage oxidation process by the following reaction:

$3FeS_2 + 8O_2 = Fe_3O_4 + 6 SO_2$ ………………………………. (6.5)

Py_1 $\quad\quad\quad$ Mag_3

The formation of magnetite veins (Mag_4) within intra-granular fractures, frequently undergoing pyrite replacement, is likely to take place during this phase.

Chalcopyrite is found as a phase intertwined with pyrrhotite and pyrite. Yund and Kullerud (1966) experimentally demonstrate the stability of a solid solution within the Cu–Fe–S system from 700°C to 334°C. Consequently, it is conceivable that chalcopyrite remained in equilibrium with the other sulfide phases during the cooling process and subsequently exsolved at a significantly later point in time.

The primary mineral composition of the migmatitic type in sample 17EG23 features garnet, along with clinopyroxene + orthopyroxene + plagioclase + antiperthite + K-feldspar ± quartz + ilmenite + pyrite, and ± chalcopyrite, accompanied by a minor presence of calcite. This comparable assembly has been documented in various high-pressure granulites (O'Brien 2008; Racek et al. 2008). Within sample 17EG24, garnet is observed forming substantial to delicate rims encircling plagioclase, orthopyroxene, and clinopyroxene grains. Porphyroblastic garnet in sample 17EG23 displays well-defined grain boundaries with orthopyroxene, plagioclase, and clinopyroxene. While explicit textural proof for garnet's presence in the apex assemblage is lacking, we propose the potential reason to be the breakdown of hornblende through the subsequent reaction:

Hornblende + plagioclase = garnet + clinopyroxene + melt …………. (6.6)

Experimental findings regarding the melting caused by the dehydration of hornblende demonstrate the stability of a residual combination of minerals comprising garnet, clinopyroxene, quartz, and Fe–Ti oxide at pressures exceeding 10 kbar (Skjerlie and PatinŏDouce, 1995). This mineral composition is associated with tonalitic to trondhjemitic melts, as established by previous studies (Beard and Lofgren, 1991; Rushmer, 1991, 1993; Wolf and Wyllie, 1994; Springer and Seck, 1997). The presence of orthopyroxene in this assemblage is suggestive of pressures below 10 kbar (Pattison, 2003). The leucosome layers within the mafic granulite samples exhibiting migmatitic characteristics potentially reveal indications of the processes of melting, the movement of molten material, and localized crystallization. Textural attributes like the presence of cuspate grain boundaries in quartz and the presence of a thin layer of K-feldspar atop plagioclase could also be interpreted as indications of the existence of melt within the system (Sawyer 1999; Brown 2001).

In the case of sample 17EG24, the emergence of a garnet (+ quartz) corona encircling orthopyroxene and clinopyroxene implies the occurrence of the following chemical transformations:

Orthopyroxene + plagioclase = garnet + quartz …………………………….. (6.7)

Clinopyroxene + plagioclase = garnet + quartz …………………….……. (6.8)

These reactions exhibit a moderately positive slope of dP/dT, indicating their potential occurrence during both cooling and loading processes. The earlier hypothesis appears more likely given the incipient nature of reaction products (garnet corona). The development of a garnet corona within migmatitic mafic granulite signifies a reduction in temperature and pressure under conditions of insufficient water (H_2O-undersaturated), during which water was primarily incorporated into the anatectic melt that largely lost from the system (Dziggel et al., 2012).

The formation of barite, replacing pyrite grains in two pyroxene granulites during the later stages, likely took place at considerably reduced temperatures, which is indicated by the sealing of brittle fractures within plagioclase grains. These partially mended fractures frequently intersect the sulphide-sulphate grains. The process of barite crystallization typically thrives in an environment with elevated oxygen levels. Carroll and Rutherford (1987) demonstrated through experimentation that the stability of sulphate phases occurs when the fO_2 condition rises to 2 units beyond the FMQ buffer. In this context, ilmenite also contains a small quantity of barium in both assemblages. As a result, variations in fO_2 took place across a broad spectrum of post-peak metamorphic temperatures within the mafic granulite.

The emergence of patchy antiperthite within plagioclase suggests the creation of the latter through a metasomatic fluid-induced process. The alteration of plagioclase involving sodium depletion and calcium enrichment may take place within a fluid predominantly composed of $CaCl_2$, via the reaction given below.

$CaCl_2$ (aq) + $2NaAlSi_3O_8$ = 2NaCl (aq) + $CaAl_2Si_2O_8$ + $4SiO_2$ …………………… (6.9)

The boundaries of this reaction have been defined through experimental means (Shmulovich and Graham 2004; Khodorevskaya and Aranovich 2016). When plagioclase interacts with aqueous fluids rich in $CaCl_2$ during retrogressive processes, the equilibrium of this reaction would be pushed towards the product formation, subsequently leading to an increased presence of NaCl within the aqueous fluid.

6.6 Geothermobarometry

Determining the pressure-temperature (P-T) conditions of metamorphism within a polymetamorphosed ultrahigh-temperature (UHT) terrain poses ongoing challenges, especially concerning mafic granulites (Huang et al. 2018). One of the primary challenges arises from the mineral composition undergoing reequilibration at lower temperatures (Frost and Chacko 1989; Harley 1989; Pattison et al., 2003). The absence of garnet within the two-pyroxene granulite assemblage poses limitations on the application of conventional geothermobarometers. The highest temperature reached during peak metamorphism was approximated using fossil thermometers, utilizing the compositional data of the dominant phases at peak conditions. In the case of sample 17EG14, the Stormer and Whitney (1977) two-feldspar thermometer yields an estimated temperature close to 870°C. The orthopyroxene–ilmenite thermometer applied to the same assemblage provides a temperature estimate of around 890°C. Employing Kretz's (1982) two-pyroxene model yields lower temperatures (Table 6.4). In contrast, for sample 17EG16, the orthopyroxene–ilmenite thermometer developed by Bishop (1980) indicates a maximum temperature of 780°C. Hornblende is an extra phase found in the assemblage of Sample 9C. The Anderson and Smith (1995) aluminium hornblende barometer measures pressure at about 7 kbar. For the same sample, the orthopyroxene-ilmenite thermometer gives a reading of 600°C. Patches of K-feldspar embedded in plagioclase in sample 17EG22 produce a temperature close to 890°C, as calculated using a two-feldspar thermometer Stormer and Whitney (1977) devised. The two-pyroxene thermometer indicates a maximum temperature of approximately 700°C, whereas the orthopyroxene–ilmenite thermometer suggests a temperature of around 785°C.

The pressure-temperature conditions have also been determined through the examination of garnet-pyroxene-bearing garnet bearing mafic granulite in samples 17EG23 and 17EG24. In the case of sample 17EG23, the assemblage comprising garnet, clinopyroxene, plagioclase, and quartz leads to a pressure estimate of approximately 7.5 kbar using the Moecher et al. (1988) model. The orthopyroxene–ilmenite thermometer indicates a temperature of around 780°C. For the same sample, applying the garnet–clinopyroxene thermometer based on Ganguly's (1979) model yields a temperature of approximately 750°C, while using Bishop's (1980) clinopyroxene–ilmenite thermometer suggests a temperature of approximately 775°C. Within sample 17EG24, the garnet–orthopyroxene thermometer devised by Lee and Ganguly (1988) suggests a maximum temperature of approximately 740°C. Meanwhile, employing the GOPQ barometer proposed by Pattison et al. (2003) provides pressure estimates in the range of 7.7–7.9 kbar. Additionally, temperature calculations were conducted for the garnet–clinopyroxene assemblage using Ganguly's (1979) model, yielding a higher maximum temperature of 830°C, surpassing the temperature estimation from the garnet–orthopyroxene thermometer.

6.7 Oxygen fugacity

Oxygen fugacity was determined through the utilization of the QUILF programme (Andersen et al. 1993), employing appropriate oxide–silicate and oxide–oxide mineral pairs from samples representing both mafic granulite assemblages (Table 6.5). The two-pyroxene granulite samples exhibit analogous mineralogical compositions (with slight disparities in oxide–sulfide arrangements) and represent the ultimate outcomes of a shared metamorphic cycle, although slight discrepancies exist in the calculated temperature and pressure values from garnet-pyroxene bearing assemblages. In order to mitigate calculation uncertainties, we have opted to utilize precise temperature values determined for each individual sample. The pressure value for every sample has been standardized at 8 kbar, taking into account the current estimations and previously published pressure-temperature records (Dasgupta et al. 1993; Bose et al. 2000, 2003). The calculation of the fO_2 value was based on the reactions that occurred among the coexisting minerals, including orthopyroxene–ilmenite, magnetite–hematite, and orthopyroxene–magnetite–quartz is given below.

$Fe_2Si_2O_6 + 2MgTiO_3 = Mg_2Si_2O_6 + 2FeTiO_3$ ………………………….. (6.10)

$4Fe_3O_4 + O_2 = 6Fe_2O_3$ …………………………………………………. (6.11)

$FeSiO_3 + O_2 = 2Fe_3O_4 + 6SiO_2$ ………………………………………… (6.12)

The oxygen fugacity values derived from these reactions exhibit an elevation of 3 to 4 logarithmic units compared to the FMQ equilibrium for samples 9C and 17EG16. However, for samples 17EG14, 17EG22, and 17EG24, oxygen fugacity values were exclusively determined through the utilization of reaction (6.10). The absence of distinct magnetite grains within the assemblage hindered the determination of fO_2 values through alternative reactions. The fO_2 values for 17EG16 were predominantly determined using equilibrium reaction (6.11), revealing a notable elevation in fO_2 (Fig. 6.28). However, there exists a solitary value for 17EG16 derived from reaction (6.12), indicating a fugacity value proximate to the graphite stability curve. Conversely, for the 17EG14 samples, a fugacity value was derived from reaction (6.10), unveiling oxygen fugacity levels that are markedly lower and situated below the graphite stability curve. The lack of identifiable individual magnetite grains and the occurrence of exsolution-free ilmenite within the mineral assemblage led to lower oxygen fugacity values that require further elucidation. Additionally, the calculated fugacity values from samples 17EG22 and 17EG24 exhibit logarithmic fO_2 values below those of the FMQ buffer. The representation of the pyrite–pyrrhotite buffer curve reaction (6.12) within figure 6.28 validates our observed textures. In both cases of samples 9C and 17EG16, pyrite exhibits prevalence over pyrrhotite; however, in the latter sample, pyrrhotite is replaced by pyrite (Py_2) and magnetite (Mag_3). Given that pyrrhotite remains stable under relatively reduced conditions, a reduction in oxygen fugacity must have occurred during the peak stage. During the retrogression of the rocks, there was an elevation in oxygen fugacity, facilitating the substitution of pyrrhotite with Py_2 and Mag_3. In contrast, all the remaining samples exhibit oxygen fugacity levels lower than the FMQ buffer, yet present textural indications that support an augmentation in oxygen fugacity—except for sample 17EG14, as shown in figure (Fig.6.28).

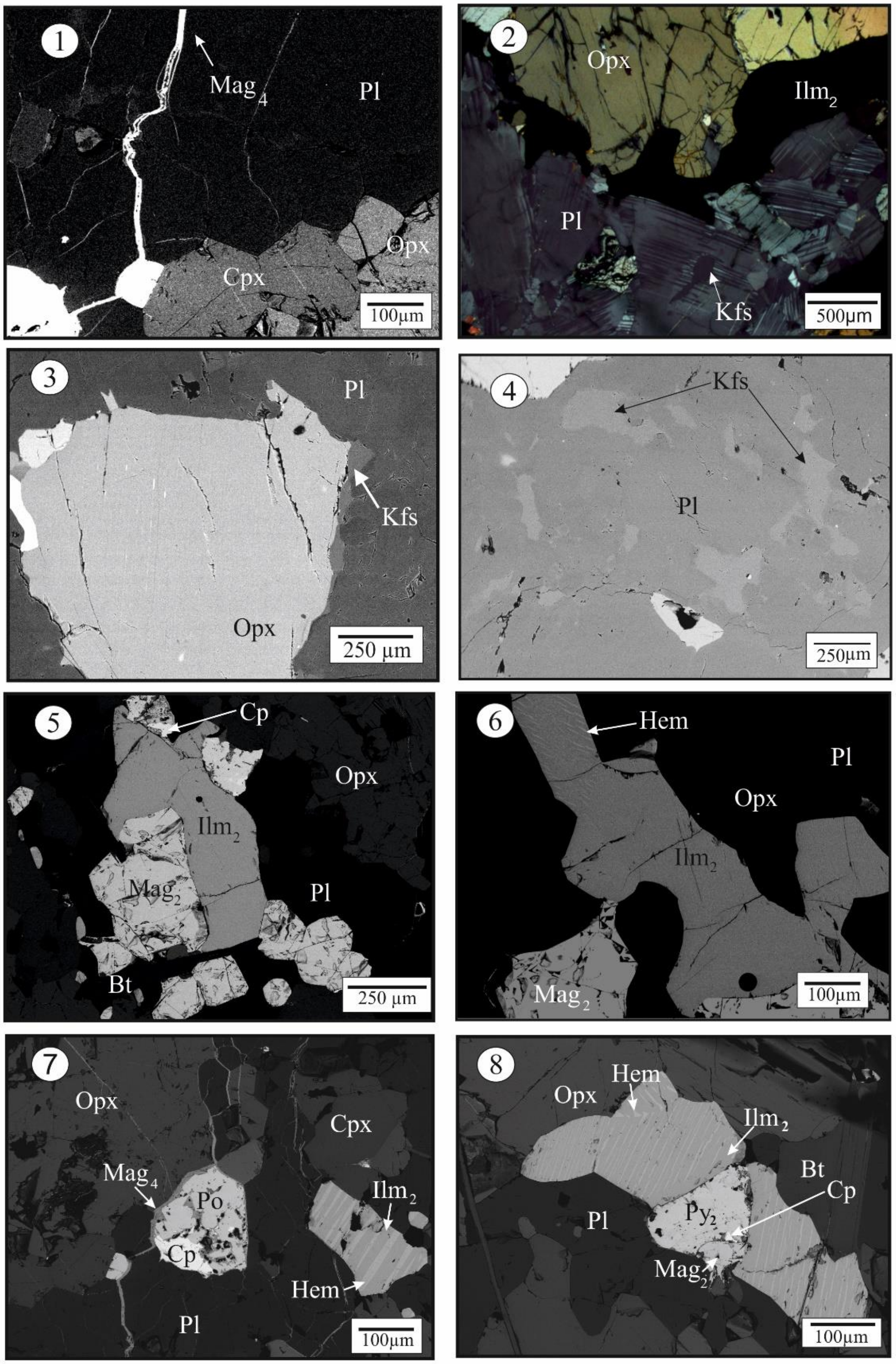

Fig. 6. Photomicrographs and BSE images of two pyroxene mafic granulite. (1) Magnetite (Mag_4) vein within plagioclase (Pl) in association with orthopyroxene (Opx) and clinopyroxene (Cpx). (2) ilmenite (Ilm_2) occurring along the margin of orthopyroxene (Opx) and antiperthitic K-feldspar (Kfs) within deformed plagioclase (Pl). (3) Thin film of K-feldspar (Kfs) along the margin of orthopyroxene (Opx). (4) Antiperthitic texture in plagioclase (Pl) where K-feldspar (Kfs) occur as patches. (5) Ilmenite (Ilm_2) partially engulfs magnetite (Mag_2). (6) Fine trellis hematite (Hem) intergrowth within ilmenite (Ilm_2). (7) Hematite (Hem) lamellae within ilmenite (Ilm_2), associated Mag_4 vein partially rims pyrrhotite (Po) and chalcopyrite (Cp). (8) Tripartite grain of magnetite (Mag_2), hemo-ilmenite (Ilm_2) and pyrite (Py) in association with plagioclase (Pl) and Opx.

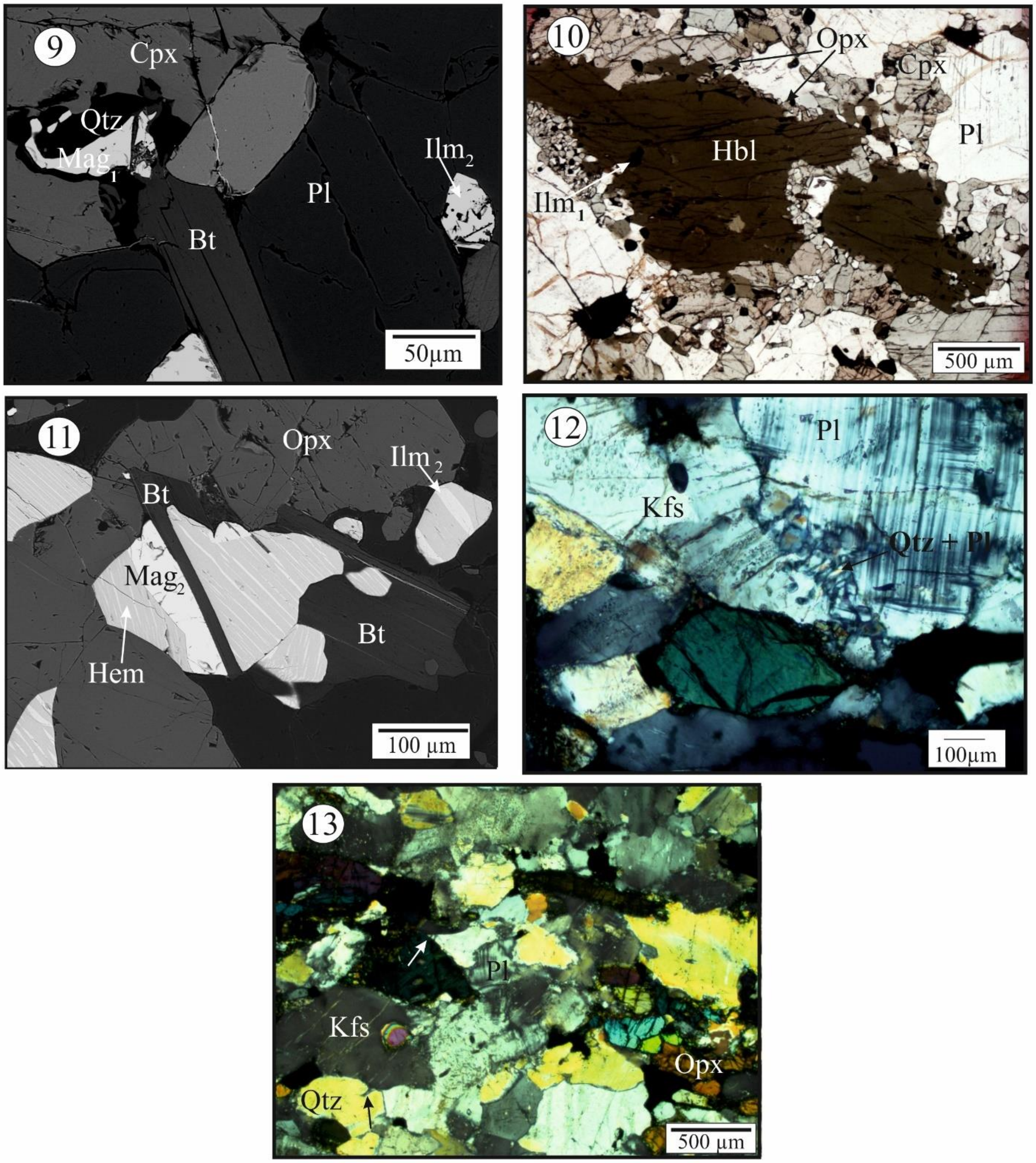

Fig. 6. Photomicrographs and BSE images of two pyroxene mafic granulite. (9) Magnetite (Mag_1) inclusion within clinopyroxene (Cpx). Note the thin rim of quartz (Qtz) separating the two. (10) Tiny grains of orthopyroxene (Opx) along the margin of hornblende (Hbl). (11) Bipartite grain of magnetite (Mag_2) and ilmenite (Ilm_2). (12) Myrmekitic intergrowth of plagioclase (Pl) and quartz (Qtz) at the margin of perthite (Kfs). (13) Cuspate grain boundaries of K-feldspar (Kfs) and quartz (Qtz) in the matrix (shown in arrows).

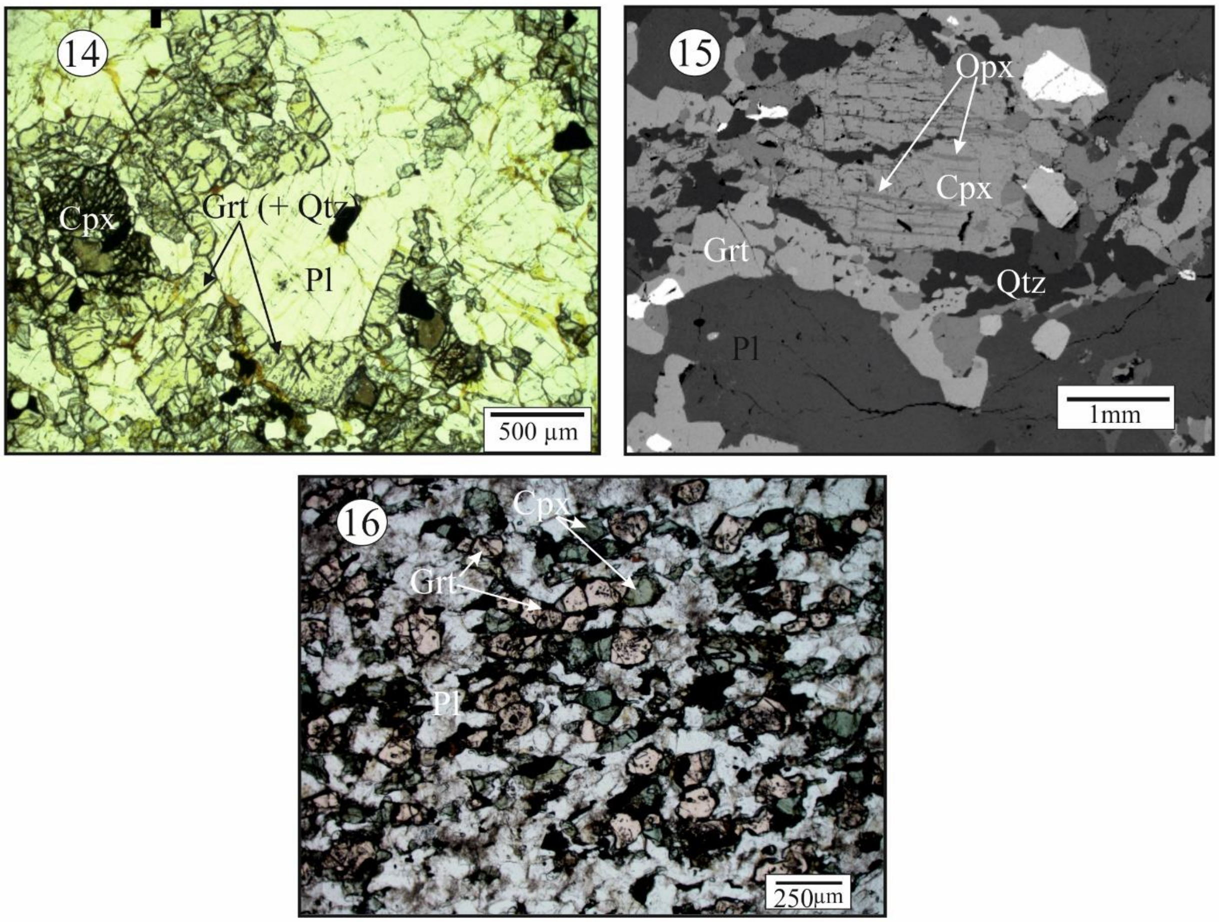

Fig. 6. Photomicrograph and BSE image of the garnet bearing mafic granulite. (14) Garnet (Grt) corona along with quartz (Qtz) around clinopyroxene (Cpx) and plagioclase (Pl). (15) Porphyroblastic clinopyroxene (Cpx) contains exsolved lamellae of orthopyroxene (Opx). (16) Porphyroblastic garnet (Grt) and Cpx grains along with Ilm_2 are stretched along the foliation.

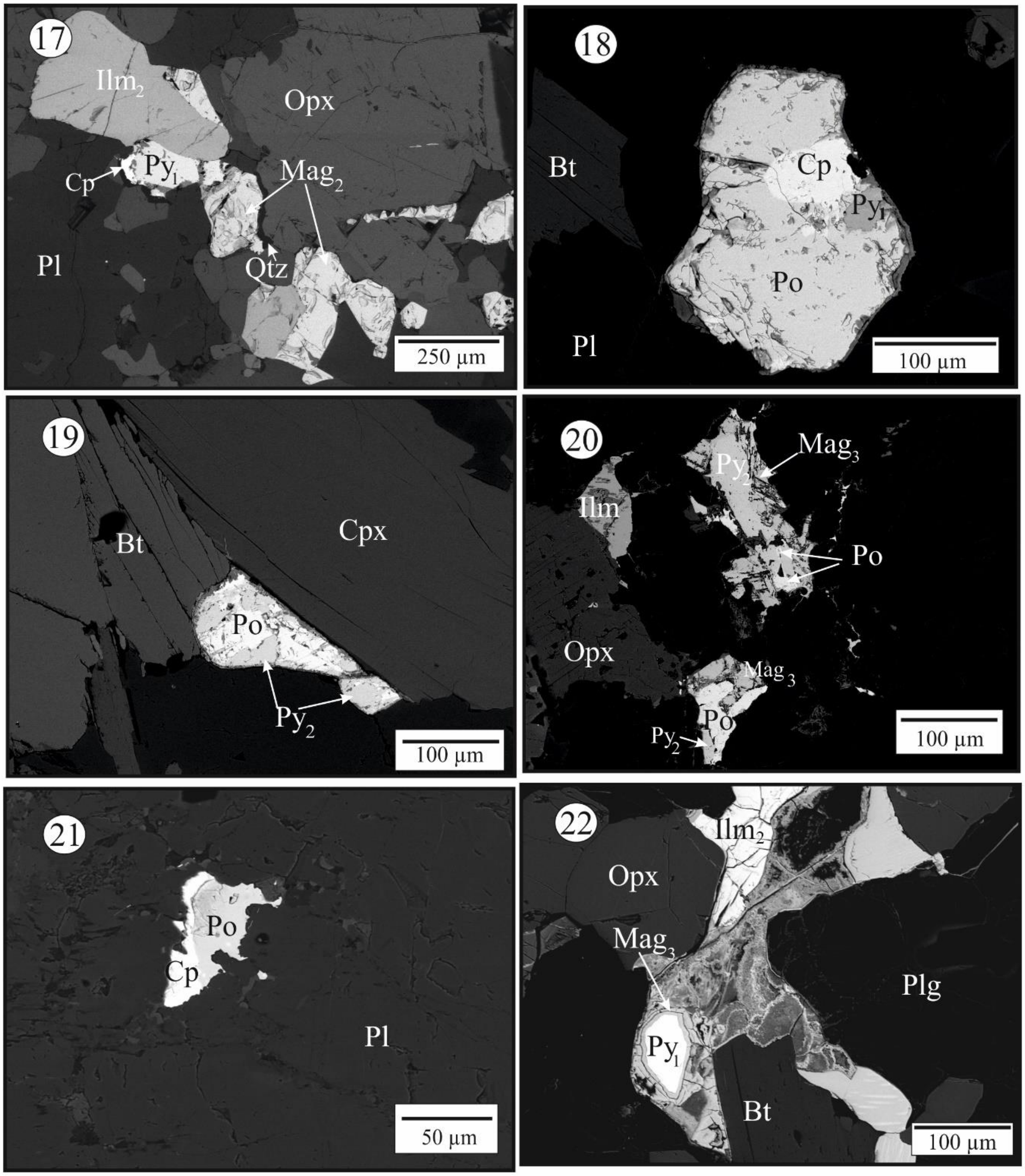

Fig. 6. BSE images showing oxide and sulphide phases of mafic granulite. (17) Pyrite (Py_1) in equilibrium contact with ilmenite (Ilm_2) and magnetite (Mag_2). (18) Relic pyrite (Py_1) within pyrrhotite (Po). Also note the tongue of chalcopyrite (Cp) in Po. (19) Pyrite (Py_2) marginally replaces pyrrhotite (Po). (20) Pyrrhotite (Po) is completely replaced by pyrite (Py_2) and magnetite (Mag_3). Note the relic of Po within Py_2. (21) Pyrrhotite (Po) and chalcopyrite (Cp) share a convolute mutual boundary within plagioclase (Pl). (22) Mantle of magnetite (Mag_3) on pyrite (Py_1).

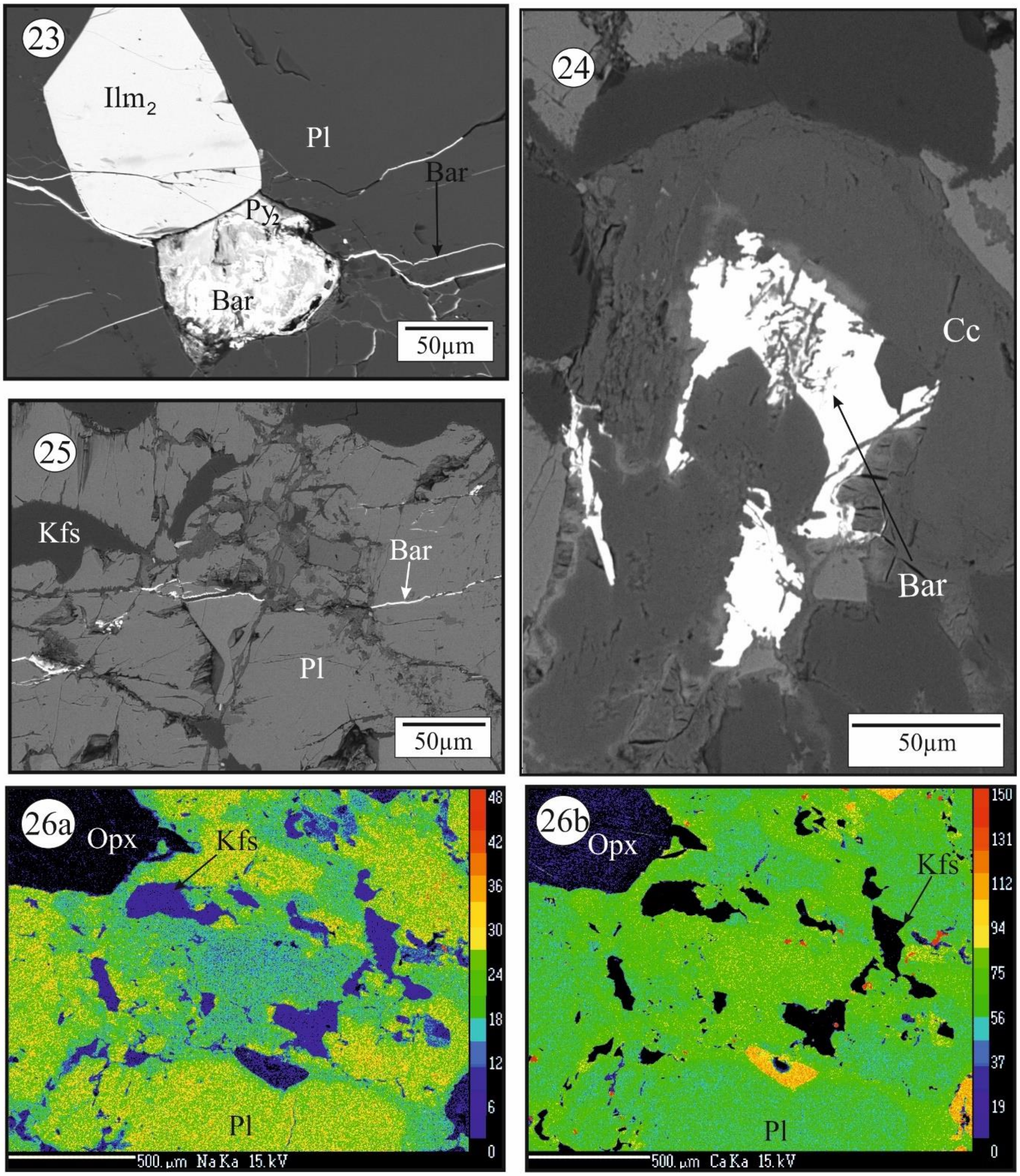

Fig. 6. BSE images showing oxide, sulphide and sulphate phases of mafic granulite. (23) Pyrite (Py_2) in contact with ilmenite (Ilm_2) is partially replaced by barite (Bar). Note the presence of thin veins containing Bar. (24) Discrete grain of calcite (Cc) and barite (Ba) in the matrix. (25) Thin barite (Bar) vein cutting through plagioclase (Pl). (26) Element X-ray map of Na (a) and Ca (b) in patchy antiperthite. The maps show Na-loss and concomitant Ca-gain of plagioclase.

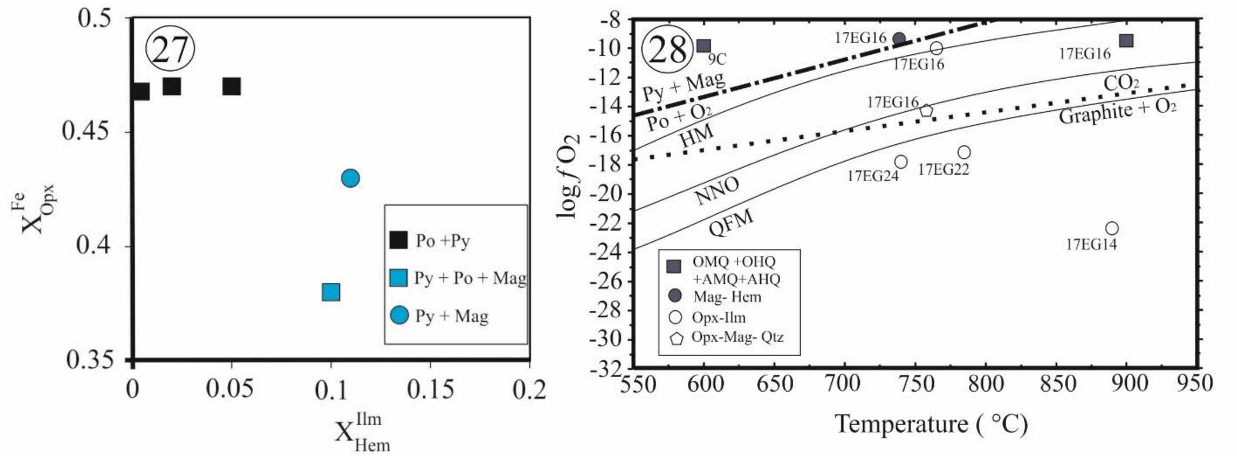

Fig. 6. (27) Plot of X^{Fe}_{Opx} vs. X^{ilm}_{Hem} shows the correlation of the oxidation states between the oxide, sulphide and silicate phases of the studied mafic granulite samples. Samples represented by black symbols are dominated by Po–Py. The blue coloured filled symbol represents samples dominated by Py–Mag with minor Po. (28) Plot of temperature vs. oxygen fugacities of the mafic granulite samples at 8 kbar. The positions of HM, NNO, CCO and QFM buffers are drawn for comparison and reference. Abbreviations used for assemblages: OMQ, orthopyroxene–magnetite–quartz; OHQ, orthopyroxene–hematite–quartz; AMQ, augite–magnetite–quartz; AHQ, augite–hematite–quartz.

Table 6.1. GPS location, mineral association and of different mafic granulite samples.

Sample no.	Rock	GPS location	Mineral association (mode%)	Structure
17EG14	Mafic granulite	18°16'58.70"N 82°57'45.30"E	Opx(31%), Cpx(11%), Pl (23%), Kfs (15%), Bt (8%), Ilm (7%), Ap (<2%), sulphide (5%, Po> Py,Cp)	Massive
17EG16	Mafic granulite	18°14'28.80"N 83° 1'49.60"E	Opx (13%), Cpx (31%), Pl (21%), Kfs (13%), Bt (3%), Mag (<3%), Ilm (9%), sulphide (5%, Py> Po, Cp), Qtz (3%)	Foliated
9C	Mafic granulite	18°19'36.50"N 83° 4'22.50"E	Opx (21%), Cpx (17%), Hbd (15%), Pl (23%), Kfs (11%), Mag (<2%), Ilm (8%), sulphide (<3 %, Py, Cp, Po)	Foliated
17EG22	Mafic granulite	18°21'36.20"N 82°44'29.10"E	Opx (21%), Cpx (15%), Pl (29%), Kfs (16%), Ilm (11%), sulphide (<7%, Po< Py, Cp)	Foliated
17EG23	Mafic granulite	18°24'06.3"N 82°40'34.4"E	Gt (17%), Opx (15%), Cpx (12%), Pl (21%), Kfs (13%), Ilm (7%), Bt (6%), Qtz (5%), sulphide (<4%. Py>Po, Cp)	Migmatitic
17EG24	Mafic granulite	18°26'41.8"N 82°40'52.2"E	Gt (13%), Opx (16%), Cpx (14%), Pl (23%), Kfs (15%), Ilm (8%), Bt (7%), Qtz (<3%), sulphide (<2% Py,Po, Cp)	Migmatitic
PLB71A	Mafic granulite	20°40'30.20"N 84°23'16.80"E	Opx (23%), Pl (27%), Kfs (19%), Bt (11%), Mag (5%), Ilm (9%), Cp (<3%).	Foliated
PLB89B	Mafic granulite	20°35'3.50"N 84°31'38.90"E	Opx (13%), Hbd (15%), Cpx (21%), Pl (23%), Kfs (17%), Mag (2%), Ilm (7%), Zrn (<2%)	Foliated
PLB93A	Mafic granulite	20°36'44.00"N 84°35'14.60"E	Gt (11%), Opx (16%), Cpx (18%), Hbd (9%), Pl (19%), Kfs (17%), Bt (5%), Qtz (<3%), Zrn (<3%)	Foliated

Table 6.2. Representative phase chemical data of two pyroxene granulite.

Rock	Two pyroxene granulite											
Sample	17EG14											
Phase	Opx		Cpx			Pl	Kfs			Ilm_2		Bt
Anal. No.:	1 (core)	2 (rim)	8 (core)	7 (rim)	30	18 (core)	37	13 (core)	34(Rim)	23 (core)	24(rim)	26 (core)
Mode	Por	Por	Por	Por	Inc Opx	Por	Patch	Por	Por	Por	Por	
SiO_2	51.22	50.53	52.34	52.39	51.65	52.84	64.58	64.69	64.81	0.03	0.03	38.12
TiO_2	0.05	0.21	0.24	0.13	0.25	0.00	0.034	0.005	0.00	51.56	52.09	5.85
Al_2O_3	1.21	1.06	1.7	1.49	1.74	29.78	18.52	19.04	18.99	0.12	0.16	12.89
Cr_2O_3	0.00	0.00	0.08	0.06	0.00					0.11	0.30	0.13
Fe_2O_3	1.89	2.32	1.61	1.49	2.90					2.61	0.00	
FeO	27.13	27.5	9.68	9.64	8.43	0.126	0.00	0.04	0.12	44.36	45.12	14.43
MnO	0.71	0.55	0.12	0.22	0.19	0.063	0.00	0.07	0.13	0.51	0.57	0.06
MgO	17.88	17.71	12.67	12.85	12.8	0.00	0.00	0.01	0.00	0.71	0.63	14.57
CaO	0.96	0.68	22.56	22.43	22.63	12.86	0.04	0.06	0.08	0.02	0.04	0.03
ZnO	0.00	0.09			0.00					0.27	0.00	0.00
Na_2O	0.07	0.01	0.33	0.27	0.34	4.47	0.57	0.65	0.63			0.05
K_2O	0.01	0.02	0.00	0.00	0.00	0.25	16.02	15.63	16.10			10.05
F												0.00
Cl												0.09
Bao							0.53	0.96	0.92	0.83	1.01	
H_2O												4.05
Total	101.13	100.68	101.32	100.96	100..91	100.39	100.30	101.19	101.78	101.16	99.32	100.78
O-basis	6	6	6	6	6	8	8	8	8	4	4	
Si	1.94	1.94	1.94	1.95	1.93	2.39	2.99	2.97	2.97	0.00	0.00	5.65
Ti	0.00	0.00	0.01	0.00	0.01	0.00	0.00	0.00	0.00	0.97	1.00	0.65
Al	0.05	0.05	0.07	0.07	0.08	1.59	1.01	1.03	1.03	0.00	0.01	2.25
Cr	0.00	0.00	0.00	0.00	0.00					0.00	0.01	0.02
Fe^{3+}	0.05	0.07	0.05	0.04	0.08					0.05	0.00	
Fe^{2+}	0.86	0.88	0.30	0.30	0.26	0.01	0.00	0.00	0.01	0.93	0.96	1.79
Mn	0.02	0.02	0.00	0.01	0.01	0.00	0.00	0.00	0.01	0.01	0.01	0.01
Mg	1.01	1.01	0.70	0.71	0.71	0.00	0.00	0.00	0.00	0.03	0.02	3.22
Ca	0.04	0.03	0.90	0.90	0.90	0.62	0.00	0.00	0.00	0.00	0.00	0.00
Zn	0.00	0.00				0.00	0.00	0.00	0.00	0.01	0.00	
Na	0.01	0.00	0.02	0.02	0.02	0.39	0.05	0.06	0.06			0.02
K	0.00	0.00	0.00	0.00	0.00	0.01	0.95	0.92	0.94			1.90
Ba							0.01	0.02	0.02	0.01	0.01	0.03
Cation												
X_{Mg}	0.54	0.53	0.70	0.70	0.73					0.028	0.024	0.99
X_{An}						0.61	0.00	0.00	0.00			
X_{Ab}						0.38	0.05	0.06	0.06			
X_{Or}						0.01	0.95	0.94	0.94			
X_{Ilm}										0.96	0.96	
X_{Hm}										0.02	0.00	
X_{Gk}										0.03	0.02	

$X_{Mg} = Mg/(Mg + Fe^{2+})$. Por, Porphyroblast; Inc, Inclusion; Disc, Discrete.

Table 6.2. Continued.

Rock	Two pyroxene granulites												
Sample		17EG16											
Phase	Bt	Opx		Cpx		Mag_2		Mag_1	Ilm_2	Ilm_1	Hem	Pl	Kfs
Anal. No.:	27 (rim)	49 (core)	50 (rim)	52 (core)	51 (rim)	53 (core)	54 (rim)	69	59 (core)	70	57	56 (core)	64
Mode		Por	Por	Por	Por	Disc.	Disc	Inc. Cpx	Por	Inc Cpx	lamellae	Por	Patch
SiO_2	38.33	51.59	51.23	50.29	50.62				0.03	0.01	0.02	49.49	63.87
TiO_2	5.19	0.04	0.07	0.38	0.38	0.14	0.04	0.35	51.14	50.68	15.79	0.02	0.03
Al_2O_3	12.99	1.21	1.41	3.15	2.74	0.40	0.31	0.32	0.15	0.18	0.24	31.64	18.19
Cr_2O_3	0.20	0.05	0.00	0.00	0.00	0.43	0.39	0.37	0.04	0.00	0.39		
Fe_2O_3		1.31	0.48	3.93	2.82	66.62	66.47	66.26	2.46	1.65	67.13		
FeO	13.75	25.09	25.57	7.43	7.58	30.50	30.09	30.65	42.39	44.44	13.64	0.51	0.03
MnO	0.04	0.55	0.68	0.32	0.30	0.00	0.09	0.08	1.39	0.83	0.06	0.00	0.00
MgO	14.98	19.39	19.17	12.38	12.51	0.12	0.11	0.02	1.23	0.04	0.25	0.00	0.00
CaO	0.00	1.05	0.61	22.29	22.41				0.02	0.18	0.06	15.01	0.06
ZnO	0.10					0.00	0.00	0.07	0.00	0.00			
Na_2O	0.07	0.04	0.02	0.45	0.42							3.16	0.26
K_2O	10.05	0.00	0.02	0.00	0.01							0.20	16.46
F	0.00												
Cl	0.11												
Bao									0.96	0.98	0.21		0.63
H_2O	4.04												
Total	100.21	100.32	99.25	100.61	99.79	98.22	97.52	98.11	98.86	99.04	97.80	100.04	99.52
O-basis		6	6	6	6	4	4	4	4	4	4	8	8
Si	5.69	1.95	1.96	1.88	1.90				0.00	0.00	0.00	2.27	2.99
Ti	0.58	0.00	0.00	0.01	0.01	0.00	0.00	0.01	0.97	0.98	0.32	0.00	0.00
Al	2.27	0.05	0.06	0.12	0.12	0.02	0.01	0.01	0.00	0.01	0.01	1.71	1.00
Cr	0.02	0.00	0.00	0.00	0.00	0.01	0.01	0.01	0.00	0.00	0.01		
Fe^{3+}		0.04	0.01	0.11	0.08	1.96	1.97	1.95	0.05	0.03	1.35		
Fe^{2+}	1.71	0.80	0.82	0.23	0.24	1.00	0.99	1.00	0.90	0.96	0.30	0.02	0.00
Mn	0.01	0.02	0.02	0.01	0.01	0.00	0.00	0.00	0.03	0.02	0.00	0.00	0.00
Mg	3.31	1.10	1.09	0.69	0.70	0.01	0.01	0.00	0.05	0.00	0.01	0.00	0.00
Ca	0.00	0.04	0.03	0.89	0.90				0.00	0.01	0.00	0.74	0.00
Zn		0.00				0.00	0.00	0.00	0.00	0.00	0.00	0.00	0.00
Na	0.02	0.00	0.00	0.03	0.03							0.28	0.02
K	1.90	0.00	0.00	0.00	0.00							0.01	0.98
Ba	0.03								0.01	0.01	0.00		0.01
Cation													
X_{Mg}	0.98	0.58	0.57	0.75	0.75	0.01	0.01	0.00	0.05	0.00	0.03		
X_{An}												0.72	0.00
X_{Ab}												0.27	0.02
X_{Or}												0.01	0.97
X_{Ilm}									0.92	0.98	0.95		
X_{Hm}									0.02	0.02	0.68		
X_{Gk}									0.05	0.00	0.03		

$X_{Mg} = Mg/(Mg + Fe^{2+})$. Por, Porphyroblast; Inc, Inclusion; Disc, Discrete.

Table 6.2. Continued.

Rock	Two pyroxene granulites												
Sample	17EG22									9C			
Phase	Opx		Cpx		Pl		Kfs		Ilm_2	Opx	Cpx	Hbd	
Anal. No.:	11 (core)	12 (rim)	13 (core)	14 (rim)	15 (core)	21	16 (core)	23	18 (core)	20 (core)	3 (core)	1 (core)	2 (rim)
Mode	Por	Por	Por	Por	Por	lamellae	Por	Patch	Por	Por	Por	Por	Por
SiO_2	50.27	50.12	51.91	51.45	53.25	54.84	64.43	64.19	0.04	51.81	50.32	40.20	41.18
TiO_2	0.08	0.00	0.26	0.22	0.00	0.00	0.01	0.00	50.16	0.07	0.33	2.07	1.86
Al_2O_3	0.90	1.33	2.2	1.76	30.29	28.85	18.94	18.81	0.14	1.51	2.78	11.68	11.20
Cr_2O_3	0.07	0.00	0.02	0.00	0.04	0.00			0.05	0.00	0.11	0.08	0.04
Fe_2O_3	0.00	0.00	2.48	1.92					2.77	2.40	4.69	3.91	4.59
FeO	32.1	31.61	12.21	11.09	0.16	0.33	0.02	0.00	43.87	23.50	5.87	11.74	10.89
MnO	0.60	0.56	0.36	0.26	0.04	0.00	0.00	0.05	0.61	0.42	0.19	0.15	0.02
MgO	14.84	15.14	10.84	11.38	0.00	0.15	0.00	0.03	0.31	20.91	13.36	11.58	12.15
CaO	0.73	0.60	21.54	22.04	12.80	10.91	0.07	0.07	0.09	0.58	22.29	11.9	11.84
ZnO	0.16	0.00	0.00	0.05		0.04			0.00	0.09	0.00	0.00	0.08
Na_2O	0.02	0.00	0.41	0.39	4.60	5.35	1.00	0.84		0.01	0.42	1.35	1.42
K_2O	0.00	0.00	0.02	0.00	0.10	0.14	15.59	15.52		0.00	0.02	2.75	2.47
F												0.00	0.00
Cl												0.79	0.67
Bao							0.59	0.62	0.87				
H_2O												1.78	1.83
Total	99.37	98.77	101.53	100.51	101.24	100.55	100.65	100..14	98.60	101.28	99.92	99.80	100.11
O-basis	6	6	6	6	8	8	8	8	4	6	6	23	23
Si	1.98	1.98	1.92	1.94	2.39	2.46	2.696	2.97	0.00	1.93	1.88	6.10	6.19
Ti	0.00	0.00	0.01	0.01	0.00	0.00	0.00	0.00	0.97	0.00	0.01	0.24	0.21
Al	0.04	0.06	0.10	0.08	1.60	1.53	1.03	1.03	0.00	0.07	0.12	2.09	1.98
Cr	0.00	0.00	0.00	0.00	0.00	0.00			0.00	0.00	0.00	0.01	0.00
Fe^{3+}	0.00	0.00	0.07	0.06					0.06	0.07	0.13	0.45	0.52
Fe^{2+}	1.06	1.04	0.38	0.35	0.01	0.012	0.00	0.00	0.93	0.73	0.18	1.49	1.37
Mn	0.02	0.02	0.01	0.01	0.00	0.00	0.00	0.00	0.01	0.03	0.01	0.02	0.00
Mg	0.87	0.89	0.61	0.64	0.00	0.01	0.00	0.00	0.01	1.162	0.74	2.62	2.72
Ca	0.03	0.03	0.87	0.89	0.62	0.53	0.00	0.00	0.00	0.02	0.89	1.93	1.91
Zn	0.16	0.00	0.00	0.00	0.00	0.00	0.00	0.00	0.00	0.00	0.00	0.00	0.01
Na	0.00	0.00	0.03	0.03	0.40	0.47	0.09	0.08			0.03	0.40	0.41
K	0.00	0.00	0.00	0.00	0.01	0.01	0.92	0.92			0.00	0.53	0.47
Ba							0.01	0.01	0.01				
Cation													
X_{Mg}	0.45	0.46	0.61	0.65					0.01	0.61	0.80	0.64	0.67
X_{An}					0.60	0.53	0.00	0.00					
X_{Ab}					0.39	0.47	0.09	0.08					
X_{Or}					0.01	0.01	0.91	0.92					
X_{Ilm}									0.96				
X_{Hm}									0.03				
X_{Gk}									0.01				

$X_{Mg} = Mg/(Mg + Fe^{2+})$. Por, Porphyroblast; Inc, Inclusion; Disc, Discrete.

Table 6.2. Continued.

Rock	Two pyroxene granulites					
Sample	9C					
Phase	Hbd	Bt	Pl	Ilm_2	Hem	Mag_2
Anal. No.:	18	8 (core)	6 (core)	13 (core)	26	47
Mode	Patch		Por	Por	lamellae	Disc.
SiO_2	41.17	37.66	47.08	0.01	0.00	
TiO_2	1.95	4.63	0.00	45.86	15.97	0.01
Al_2O_3	11.60	12.51	32.93	0.16	0.25	0.58
Cr_2O_3	0.16	0.00		0.21	0.63	0.34
Fe_2O_3	2.86			11.09	67.5	67.82
FeO	12.17	12.45	0.31	40.05	13.98	30.85
MnO	0.00	0.09	0.00	0.44	0.00	0.03
MgO	11.87	17.16	0.00	0.37	0.21	0.09
CaO	12.14	0.10	17.02	0.08	0.00	0.00
ZnO	0.06	0.00		0.00		0.08
Na_2O	1.43	0.10	2.18	0.00		0.00
K_2O	2.41	9.82	0.11	0.04		0.00
F	0.00	0.00				
Cl	0.64	0.33				
Bao				0.86	0.27	
H_2O	1.83	3.92				
Total	100.16	98.71	99.63	98.01	98.55	99.8
O-basis	23	11	8	4	4	4
Si	6.19	5.64	2.72	0.00	0.00	0.00
Ti	0.22	0.52	0.00	0.89	0.32	0.00
Al	2.06	2.21	1.79	0.01	0.01	0.03
Cr	0.02	0.00	0.00	0.00	0.01	0.01
Fe^{3+}	0.32	0.00	0.00	0.22	1.34	1.96
Fe^{2+}	1.53	1.60	0.01	0.85	0.31	0.99
Mn	0.00	0.01	0.00	0.01	0.00	0.00
Mg	2.66	3.83	0.00	0.01	0.01	0.01
Ca	1.95	0.02	0.84	0.00	0.00	0.00
Zn	0.01	0.00	0.00	0.00	0.00	0.00
Na	0.42	0.03	0.20			0.00
K	0.46	1.88	0.01			0.00
Ba				0.01	0.00	
Cation						
X_{Mg}	0.64	0.71		0.02	0.03	0.01
X_{An}			0.81			
X_{Ab}			0.19			
X_{Or}			0.01			
X_{Ilm}				0.96	0.97	
X_{Hm}				0.11	0.67	
X_{Gk}				0.02	0.03	

$X_{Mg} = Mg/(Mg + Fe^{2+})$. Por, Porphyroblast; Inc, Inclusion; Disc, Discrete.

Table 6.3. Representative phase chemical data of garnet bearing mafic granulite.

Rock	Garnet-pyroxene granulites											
Sample	17EG23							17EG24				
Phase	Grt		Bt	Cpx	Ilm_2	Kfs	Pl	Grt		Opx		Cpx
Anal. No.:	1	6	13	2 (core)	10 (core)	18	9 (core)	47 (Core)	48 (rim)	20 (core)	24	15 (core)
Mode	Crn.	Crn.	Inc. (G)	Por.	Disc.	Rim	Por.	Por.	Por.	Por	lamellae	Por
SiO_2	37.84	38.35	38.75	51.16	0.03	64.13	57.419	37.62	37.87	51.34	50.79	51.75
TiO_2	0.03	0.02	5.37	0.22	51.53	0.00	0	0.04	0.02	0.08	0.08	0.20
Al_2O_3	21.32	21.77	13.24	1.73	0.16	18.63	26.287	21.58	21.60	0.85	1.08	1.96
Cr_2O_3	0.00	0.08	0.12	0.00	0.01	0.00	0.00	0.13	0.00	0.03	0.00	0.02
Fe_2O_3	1.47	0.89	0.00	4.15	1.58	0.00	0.00	2.78	2.60	1.95	2.62	4.26
FeO	26.74	27.28	12.83	7.82	44.20	0.11	0.12	26.39	27.14	28.59	28.24	8.20
MnO	1.17	1.01	0.11	0.04	0.29	0.00	0.01	1.00	0.97	0.17	0.37	0.14
MgO	4.65	4.79	17.08	12.61	1.01	0.00	0.02	4.54	4.45	17.91	17.55	12.62
CaO	7.07	7.05	0.01	22.56	0.06	0.09	8.73	7.44	7.21	0.55	0.69	22.54
ZnO	0.00	0.00	0.00	0.00	0.00	0.00	0.00	0.00	0.00	0.06	0.04	0.00
Na_2O	0.00	0.00	0.11	0.46	0.00	1.02	6.87	0.00	0.00	0.00	0.00	0.51
K_2O	0.00	0.00	10.14	0.00	0.00	15.27	0.22	0.00	0.00	0.00	0.00	0.00
F	0.00	0.00	0.00	0.00	0.00	0.00	0.00	0.00	0.00	0.00	0.00	0.00
Cl	0.00	0.00	0.15	0.00	0.00	0.00	0.00	0.00	0.00	0.00	0.00	0.00
Bao					0.94	0.82	0.00					
H2O			4.19									
Total	100.28	101.23	101.97	100.75	99.64	99.23	99.68	101.51	101.86	101.54	101.46	102.19
O-basis	12	12	11	6	4	8	8	12	12	6	6	6
Si	2.70	2.98	5.61	1.91	0.00	2.98	2.59	2.92	2.94	1.95	1.94	1.91
Ti	0.00	0.00	0.59	0.01	0.98	0.00	0.00	0.00	0.00	0.00	0.00	0.01
Al	1.97	1.99	2.26	0.08	0.01	1.02	1.40	1.98	1.97	0.04	0.05	0.09
Cr	0.00	0.01	0.00	0.00	0.00	0.00	0.00	0.01	0.00	0.00	0.00	0.00
Fe^{3+}	0.09	0.05	0.00	0.12	0.04	0.00	0.00	0.16	0.15	0.06	0.08	0.12
Fe^{2+}	1.76	1.77	1.55	0.25	0.92	0.00	0.00	1.72	1.76	0.91	0.90	0.25
Mn	0.08	0.07	0.01	0.00	0.01	0.00	0.00	0.07	0.06	0.01	0.01	0.00
Mg	0.54	0.55	3.69	0.70	0.04	0.00	0.00	0.53	0.51	1.02	1.00	0.69
Ca	0.59	0.59	0.00	0.90	0.00	0.01	0.42	0.62	0.60	0.02	0.03	0.89
Zn			0.00	0.00			0.00			0.00	0.00	
Na			0.03	0.03	0.04	0.09	0.60					0.04
K			1.87	0.00	0.96	0.91	0.01					0.00
Ba					0.01	0.01						
Cation												
X_{Mg}	0.24	0.24	0.70	0.74	0.04			0.24	0.23	0.53	0.53	0.73
X_{An}						0.01	0.41					
X_{Ab}						0.09	0.58					
X_{Or}						0.90	0.01					
X_{Ilm}					0.94							
X_{Hm}					0.02							
X_{Gk}					0.04							
X_{Prp}	0.18	0.18						0.17	0.17			
X_{Alm}	0.60	0.60						0.61	0.62			
X_{Grs}	0.19	0.19						0.20	0.19			
X_{Sps}	0.03	0.02						0.02	0.02			

$X_{Mg} = Mg/(Mg + Fe^{2+})$. Crn, Coronal phase;Por, Porphyroblast; Disc, Discrete.

Table 6.3: Continued.

Rock	Garnet-pyroxene granulites					
Sample						
Phase	Cpx	Pl		Kfs	Ilm_2	
Anal. No.:	16 (rim)	40 (core)	41 (rim)	37 (core)	9 (core)	10 (rim)
Mode	Por	Por	Por	Por	Disc.	Disc.
SiO_2	51.65	55.78	55.62	65.22	0.00	0.00
TiO_2	0.07	0.00	0.07	0.00	52.73	51.14
Al_2O_3	1.70	28.23	27.75	18.86	0.21	0.11
Cr_2O_3	0.04				0.10	0.07
Fe_2O_3	2.88				2.86	5.06
FeO	9.06	0.09	0.14	0.05	44.74	43.9
MnO	0.08	0.03	0.01	0.00	0.43	0.16
MgO	12.74	0.03	0.02	0.04	1.24	0.98
CaO	22.93	10.87	10.35	0.13	0.02	0.02
ZnO	0.00				0.01	0.16
Na_2O	0.13	5.80	6.19	1.72		
K_2O	0.00	0.19	0.14	14.07		
F	0.00					
Cl	0.00					
Bao						
H2O						
Total	101.27	101.03	100.28	100.13	102.32	101.45
O-basis	6	8	8	8	4	4
Si	1.92	2.49	2.50	2.99	0.00	0.00
Ti	0.00	0.00	0.00	0.00	0.97	0.95
Al	0.08	1.49	1.47	1.02	0.01	0.00
Cr	0.00				0.00	0.00
Fe^{3+}	0.08				0.05	0.09
Fe^{2+}	0.28	0.00	0.01	0.00	0.92	0.91
Mn	0.00	0.00	0.00	0.00	0.01	0.00
Mg	0.71	0.00	0.00	0.00	0.05	0.04
Ca	0.92	0.52	0.50	0.01	0.00	0.00
Zn					0.00	0.00
Na	0.01	0.50	0.54	0.16		
K	0.00	0.01	0.01	0.82		
Ba				0.01		
Cation						
X_{Mg}	0.72				0.05	0.04
X_{An}		0.5	0.48	0.01		
X_{Ab}		0.49	0.52	0.16		
X_{Or}		0.01	0.01	0.84		
X_{Ilm}					0.94	0.95
X_{Hm}					0.03	0.05
X_{Gk}					0.05	0.04
X_{Prp}						
X_{Alm}						
X_{Grs}						
X_{Sps}						

$X_{Mg} = Mg/(Mg + Fe^{2+})$. Crn, Coronal phase;Por, Porphyroblast; Disc, Discrete.

Table 6.4. Thermobarometric results from representative samples of mafic granulite.

Sample No.	Thermo/barometer used	Model	Assumed P/T	Result
17EG14	Opx- Ilm thermometer	Bishop, (1980)	8.0 kbar	890 °C
	Cpx-Ilm thermometer	Bishop, (1980)	8.0 kbar	733.42 °C
	2Pyroxene Thermometer	Kretz, (1982)		677.39 °C
	2 Feldspar Thermometer	Stormer, (1975)	8.0 kbar	869.51 °C
17EG16	Opx-Ilm thermometer	Bishop, (1980)	8.0 kbar	777.82 °C
	2Pyroxene Thermometer	Kretz, (1982)		685.56 °C
9C	Al-in-hornblende barometers	Anderson and Smith, (1995)	600 °C	7.15 kbar
	Cpx-Ilm thermometer	Bishop, (1980)	8.0 kbar	536.24 °C
	Opx-Ilm thermometer	Bishop, (1980)	8.0 kbar	612.49 °C
17EG22	Opx- Ilm thermometer	Bishop, (1980)	8.0 kbar	784.92 °C
	Cpx-Ilm thermometer	Bishop, (1980)	8.0 kbar	608.52 °C
	2Pyroxene Thermometer	Kretz, (1982)		703.72 °C
	2 Feldspar Thermometer	Stormer, (1975)	8.0 kbar	891.54 °C
17EG23	Gt-Cpx geothermometer	Ganguly, (1979)	8.0 kbar	749.85 °C
	Cpx- Ilm thermometer	Bishop, (1980)	8.0 kbar	772.69 °C
	GCPS (Di- barometer)	Moecher *et al* .,(1988)	780 °C	7.5 kbar
17EG24	Gt-Opx geothermometer	Lee & Ganguly,(1988)	8.0 kbar	741.16 °C
	GOPQ, RCLC	Pattison *et al* ., (2003)	7.97 kbar	672 °C
	Gt-Cpx thermometer	Ganguly, (1979)	8.0 kbar	779.59 °C
	Gt-Ilm thermometer	Pownceby *et al* ., (1987)		544.65 °C
	Cpx-Ilm thermometer	Bishop, (1980)	8.0 kbar	726.39 °C
	GCPS (Di- barometer)	Moecher,Essene & Anovitz, (1988)	765 °C	7.8 kbar

Table 6.5. Oxygen fugacity values calculated at estimated pressure and temperature (as discussed in the text; QUILF reactions are after Andersen et al., 1993).

Sample	**Oxide- silicate/oxide pairs**	**Temperature**	**Pressure**	**log *f* O2**	**ΔFMQ**
17EG14	Opx-Ilm $Fe_2Si_2O_6+2MgTiO_3= Mg_2Si_2O_6+2FeTiO_3$	890 °C	8 kbar	-22.35	-10.31
17EG16	Opx-Ilm	765 °C	8 kbar	-10.01	4.52
	Mag-Hem $4Fe_3O_4 + O_2= 6Fe_2O_3$	765 °C	8 kbar	-9.99	4.53
	Opx-Mag-Qtz + Opx-Hem-Qtz + Aug-Mag-qtz + Aug-Hem-Qtz $3Fe_2Si_2O_6 + O_2= 2Fe_3O_4 + 6SiO_2$. $2Fe_2Si_2O_6 + O_2= 2Fe_2O_3 + 4SiO_2$	900 °C	8 kbar	-9.45	4.59
9C	Opx-Mag-Qtz + Opx-Hem-qtz + Aug-Mag-Qtz + Aug-Hem-Qtz	600 °C	8 kbar	-9.84	4.50
17EG22	Opx-Ilm	785 °C	8 kbar	-17.14	-3.05
17EG24	Opx-Ilm	740 °C	8 kbar	-17.79	-2.69